



Layer number and stacking order dependent thermal transport in molybdenum disulfide with sulfur vacancies

Ranjuna M K ^{*} and Jayakumar Balakrishnan [†]

Department of Physics, Indian Institute of Technology Palakkad, Palakkad 678623, Kerala, India



(Received 12 June 2023; revised 27 November 2023; accepted 28 November 2023; published 13 December 2023)

Recent theoretical works on two-dimensional molybdenum disulfide (MoS_2) with sulfur vacancies predict that the suppression of thermal transport in MoS_2 by point defects is more prominent in monolayers and becomes negligible as the layer number increases. Here, we investigate experimentally the thermal transport properties of two-dimensional (2D) molybdenum disulfide crystals with inherent sulfur vacancies. We study the first-order temperature coefficients of interlayer and intralayer Raman modes of MoS_2 crystals with different layer numbers and stacking orders. The in-plane thermal conductivity (κ) and total interface conductance per unit area (g) across the 2D material-substrate interface of mono-, bi-, and trilayer MoS_2 samples are measured using micro-Raman thermometry. Our results clearly demonstrate that the thermal conductivity is significantly suppressed by sulfur vacancies in monolayer MoS_2 . However, this reduction in κ becomes less evident as the layer number increases, confirming the theoretical predictions. No significant variation is observed in the κ and g values of $2H$ and $3R$ stacked bilayer MoS_2 samples.

DOI: [10.1103/PhysRevB.108.245411](https://doi.org/10.1103/PhysRevB.108.245411)

I. INTRODUCTION

Two-dimensional (2D) transition metal dichalcogenides (TMDs), an advancing class of layered materials, have recently become a fertile ground for investigating fundamental properties and emergent device applications. Among these, 2D crystals of molybdenum disulfide (MoS_2) have gained significant importance due to their unique properties, such as direct band gaps in monolayers [1], high carrier mobility, significant light-matter interactions [2], reasonable spin-orbit interactions [3], good valley selectivity [4–6], and a high Seebeck coefficient [7–9]. This makes them potential materials for applications in electronics [10–12], optoelectronics [13–15], valleytronics [4,5,16], and energy harvesting [9,17]. However, the number and stacking order of layers and the defects and impurities in MoS_2 can significantly impact its properties and the device's performance [18].

Monolayer MoS_2 comprises the hexagonal arrangement of molybdenum (Mo) and sulfur (S) atoms sandwiched to form an S-Mo-S structure. These monolayers can be stacked in different configurations to form different polytypes of multilayer MoS_2 . Previous studies on the most common configurations, the $2H$ (hexagonal) and $3R$ (rhombohedral) phases, reveal that stacking order is vital in various applications such as piezoelectricity, nonlinear optics, and catalytic activity [19–21]. Similarly, structural defects in MoS_2 , such as vacancies, substitutions, dislocations, grain boundaries, and edges, can significantly influence its properties due to their impact on the atomic structure and electronic behavior [11,18,22,23]. However, depending on the targeted application, their impact

can be either detrimental or beneficial. For example, the mobility of carriers in electronic devices can get reduced by the collision with defects. In contrast, the presence of defects can enhance the performance of MoS_2 in various fields, including catalysis, energy storage, and sensing [17].

Understanding the effect of stacking order and structural defects on thermal transport in MoS_2 is crucial for optimizing its thermal properties and thermoelectric applications and designing efficient thermal management strategies in various applications. The thermal conductivity of monolayer and multilayer MoS_2 in its suspended and substrate-bound form has been reported [24–27]. However, most of these works do not account for the possibility of structural defects or differences in the stacking order of MoS_2 crystals. Recently, there have been theoretical studies on the thermal transport in MoS_2 with various defects such as grain boundaries, vacancies, and substitutions [28–35]. A recent experimental work explored the phonon thermal transport in few-layer MoS_2 flakes with various point defect concentrations enabled by helium ion (He^+) irradiation [36]. They observed that Mo vacancies significantly reduce the thermal conductivity of few-layer MoS_2 compared to S vacancies. Similarly, recent work on thermal transport in chemical vapor deposition (CVD)-grown monolayer MoS_2 with grain boundaries also showed a lower thermal conductivity of the sample [37].

In this paper, we report a systematic study of thickness dependent thermal transport in supported MoS_2 crystals with sulfur vacancies, including the $2H$ and $3R$ stacked bilayers. The in-plane thermal conductivity (κ) and total interface conductance per unit area (g) across the 2D material-substrate interface are obtained using Raman thermometry. For this, in the first part of this paper, we provide a detailed analysis of the first-order temperature coefficients for both intra- and

*ranjuna.mk@gmail.com

†jayakumar@iitpkd.ac.in

interlayer Raman modes. Here, we will report on the evolution of first-order temperature coefficients of low-frequency interlayer Raman modes of MoS₂ with layer number. In the second part, we utilize the first-order temperature coefficient of the Raman mode to calibrate the sample temperature during laser heating and, consequently, determine the thermal transport parameters of the sample. Our experimental results show that the κ decreases as the layer number increases, whereas the g increases. Our results also demonstrate that the thermal conductivity is significantly suppressed by sulfur vacancies in monolayer MoS₂. However, this reduction in κ becomes less evident as the layer number increases. Hence our results confirm the recent theoretical predictions that the suppression of thermal transport in MoS₂ by point defects is more prominent in monolayers and becomes negligible as the layer number increases due to the smaller density of the sulfur vacancies. No significant variation is observed in the κ and g values of the 2H and 3R stacked bilayer MoS₂ samples.

II. RESULTS AND DISCUSSIONS

The 2D crystals of MoS₂ samples are prepared from a bulk crystal by mechanical exfoliation and transferred on silicon wafers covered by 285-nm-thick SiO₂. The numbers of MoS₂ layers are first identified by optical contrast and then confirmed by Raman spectroscopy. The stacking order of bi- and trilayer samples is determined using interlayer phonon modes in their Raman spectra. Previous works identified sulphur vacancies as the dominant category of defects in mechanically exfoliated MoS₂ samples [38]. In our work, the exfoliated MoS₂ samples are annealed in an H₂-Ar environment for 3 h at 350 °C. It has been shown that the annealing of MoS₂ crystals in an H₂-Ar environment above 300 °C results in the creation of additional sulfur vacancies [39]. The stoichiometry of the molybdenum disulfide (Mo:S ratio) is obtained in the range of 1:1.70–1:1.93 from scanning electron microscopy energy dispersive spectroscopy (SEM-EDS) and in the range of 1:1.71–1:1.76 from the x-ray photoelectron spectroscopy (XPS) measurement which confirms the presence of sulfur vacancies in the sample [40]. The 15% sulfur vacancies corresponding to a stoichiometric ratio of 1:1.7 are considered as the upper limit since the exposed area covers the sample edges. To confirm further, a transmission electron microscopy–energy dispersive spectroscopy (TEM-EDS) analysis is performed, and an Mo:S ratio of 1:1.80 is obtained. Additional details on sample preparation and characterization can be found in Ref. [40] and in the Supplemental Material [41].

The thermal transport properties of 2D crystals of MoS₂ are measured using Raman thermometry [43]. This method benefits from its noncontact and nondestructive nature and relatively simple implementation. The experiment involves the application of a localized heat source to the material and measuring the resulting temperature changes. In the context of optothermal Raman techniques, the first-order temperature coefficient can serve as a valuable tool for calibrating the average sample temperature when exposed to laser heating. Later, a steady-state heat conduction model is used to extract the κ and g values of the 2D materials bound to a substrate.

Initially, a low-power ($\sim 200 \mu\text{W}$) 532-nm laser beam is used to acquire the Raman spectra of uniformly heated MoS₂ samples at different temperatures. Figures 1(a)–1(e) represent the Raman spectra of MoS₂ samples recorded at different temperatures. The peaks around 384 and 406 cm⁻¹ correspond to the intralayer E_{2g}^1 and A_{1g} modes, respectively. The E_{2g}^1 mode originates from the in-plane vibrations of the molybdenum (Mo) and sulfur (S) atoms, and the A_{1g} mode originates from the out-of-plane vibrations of S atoms [44]. In all samples, the Raman mode frequency redshifts with increased temperature, as shown in Figs. 1(a)–1(e). This observed redshift in phonon frequency is mainly due to the contribution from thermal expansion and anharmonic coupling of phonon modes at higher temperatures [25]. The Raman mode frequencies corresponding to an increase in temperature are fitted with a linear function [$\omega(T) = \omega_0 + \chi_T \times T$] to determine the first-order temperature coefficient (χ_T) of each phonon mode. A comparison of the first-order temperature coefficient of E_{2g}^1 and A_{1g} modes of MoS₂ flakes with different layer numbers and stacking orders is provided in Fig. 2. For all layer numbers and stacking orders under study, the magnitude of the χ_T value of the E_{2g}^1 mode is higher than that of the A_{1g} mode, which agrees with previous reports [25,45]. This difference in temperature coefficients between the E_{2g}^1 and A_{1g} Raman modes in MoS₂ can be attributed to their different symmetries and vibrational characteristics. Since the E_{2g}^1 mode corresponds to the in-plane vibration of S and Mo atoms, it is particularly sensitive to the thermal expansion and anharmonic effects in the in-plane direction, contributing to its higher-temperature coefficient. We observed that the χ_T values of the E_{2g}^1 mode exhibited a monotonous decrease in its magnitude as the layer number increased, whereas that of the A_{1g} mode exhibited a sharp reduction from monolayer to bilayer and then increased with layer number.

Other than the E_{2g}^1 and A_{1g} modes, the Raman spectrum of the MoS₂ samples contains interlayer phonon modes that appear in the low-frequency range (below 50 cm⁻¹). The shear mode (SM) and layer breathing mode (LBM) originate from the in-plane and out-of-plane vibrations of both S and Mo atoms, respectively, as shown in Fig. 3(a). These modes are absent in the monolayer. The temperature coefficients of these interlayer modes in MoS₂ are not extensively studied as other Raman modes, primarily due to their relatively weaker intensity and the requisite of a more complex experimental setup with access to ultralow frequencies and better spectral resolution [45,46]. Here, we analyze the temperature dependence of the low-frequency Raman modes of bi-, tri-, and few-layer MoS₂ flakes. Figure 3(b) displays the variation in the peak position of the low-frequency modes as a function of temperature and the values of the first-order temperature coefficients are given in Table SI [41]. Both shear and layer breathing modes show redshifts due to anharmonicity and thermal expansion at higher temperatures [46]. However, the χ_T values of the interlayer modes are much smaller than those of the high-frequency intralayer modes since these layers are coupled via a weak van der Waals force. The thermal expansion along the out-of-plane direction is negligible because the effect of temperature on the interlayer distance is considerably weak. Therefore, the contribution of crystal thermal expansion to the temperature coefficient can be ignored

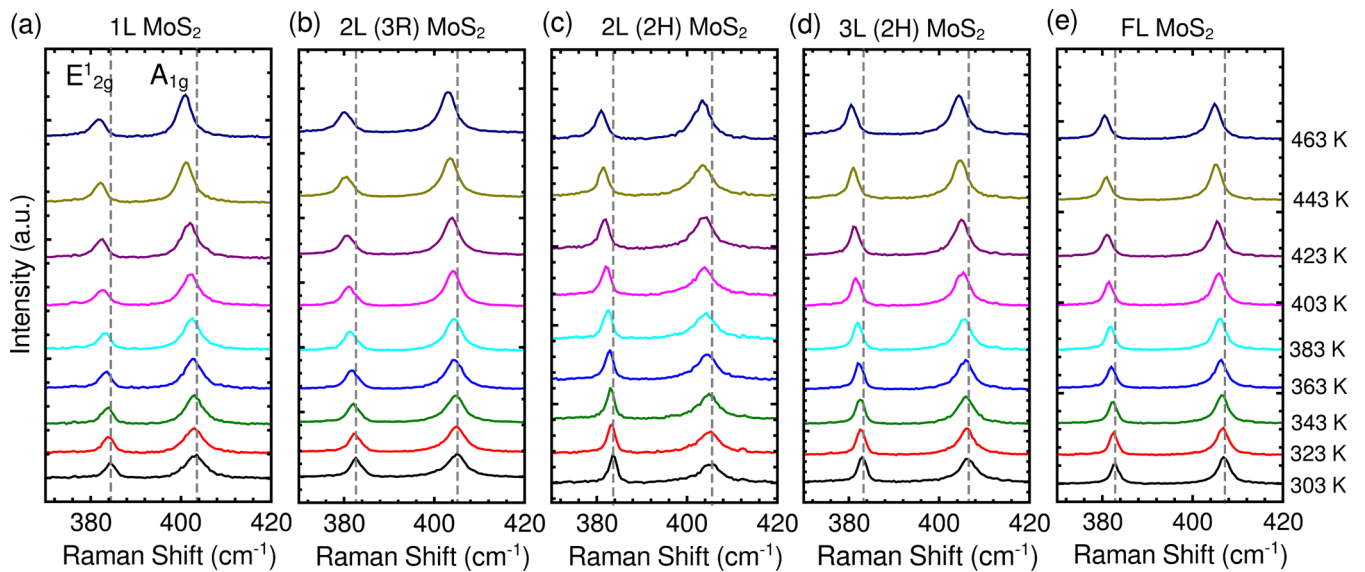


FIG. 1. The high-frequency range of the Raman spectrum acquired at different temperatures using a 532-nm excitation wavelength for (a) monolayer, (b), (c) bilayer, (d) trilayer, and (e) few-layer MoS₂ crystals exfoliated on a Si/SiO₂ substrate. The dashed vertical lines indicate the position of E_{2g}¹ and A_{1g} modes at 303 K.

for the layer breathing mode [45]. This justifies the small temperature coefficient value of the layer breathing mode. In contrast, the shear mode is affected by thermal expansion, giving rise to a relatively larger temperature coefficient than the breathing mode. Additionally, the temperature coefficients of the low-frequency modes can also depend on the interlayer interaction strength. The difference in the first-order temperature coefficient of the shear mode for 2H and 3R polytypes could be a manifestation of the difference in their interlayer coupling strength. The χ_T value of the shear mode reduces their magnitude as the layer number increases.

Since both E_{2g}¹ and A_{1g} modes have higher-temperature coefficients, it allows for the measurement of the local temperature rise of the supported MoS₂ crystals due to a change in the incident laser power by employing changes in the phonon frequency. Raman measurements are performed with different laser powers for two different spot-size objectives in

ambient conditions. A 532-nm laser excitation is used with a step variable neutral density filter and 1800 lines/mm grating. The incident power is measured with a power meter, and the absorbed power is calculated by considering the layer number dependent optical absorption for the 532-nm wavelength. The variation of the peak position of E_{2g}¹ and A_{1g} phonon modes with absorbed laser power is displayed in Fig. 4. For all samples, the peak position redshifts with increased absorbed laser power. The fitting of data points with a linear function gives the power coefficient ($d\omega/dQ = \chi_p$) of each Raman mode. The χ_p of the A_{1g} mode appears more sensitive to variations in layer number than that of the E_{2g}¹ mode (Fig. S3 [41]). Since the A_{1g} mode is insensitive to in-plane strain and its power coefficient is more sensitive to layer number, the temperature-induced softening of the A_{1g} phonon mode is

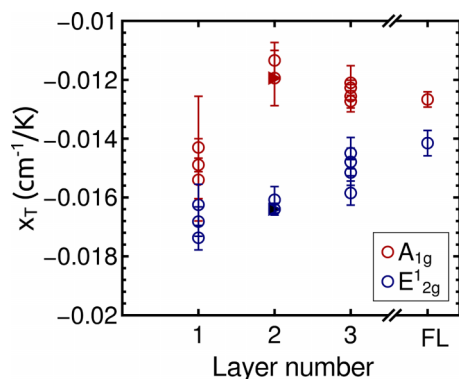


FIG. 2. The value of the first-order temperature coefficient of E_{2g}¹ and A_{1g} modes for mono-, bi-, tri-, and few-layer MoS₂ crystals on a Si/SiO₂ substrate. Different data points indicate different samples and the triangles indicate a 3R stacked bilayer.

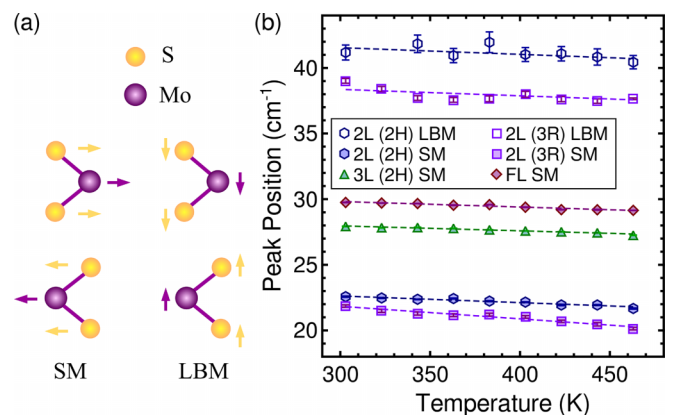


FIG. 3. (a) Schematic of the interlayer vibrational modes of MoS₂. (b) The peak position of the layer breathing mode (LBM) and shear mode (SM) at different temperatures for bi-, tri-, and few layer MoS₂ crystals exfoliated on a Si/SiO₂ substrate (X and Y axis in linear scale). The dashed lines represent a linear fit to the data points.

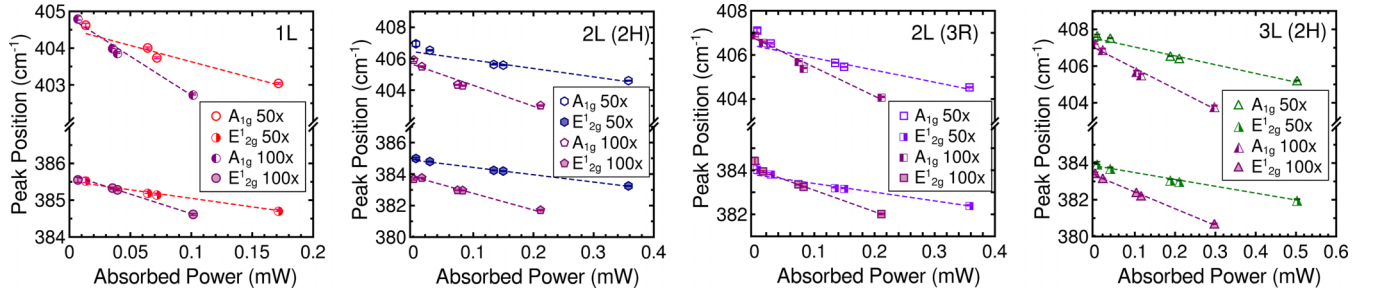


FIG. 4. The peak position of the A_{1g} and E_{2g}^1 phonon modes at different absorbed laser powers for mono-, bi-, and trilayer MoS_2 crystals exfoliated on a Si/SiO_2 substrate (X and Y axis in linear scale). The dashed lines represent linear fit to data points.

used to estimate the local temperature rise and extract the thermal parameters.

The modeling of thermal transport in supported 2D materials subjected to laser heating has been reported previously [43,47,48]. A laser beam with a Gaussian intensity distribution is used for the local heating of the sample, as shown in Fig. 5. Under the steady-state condition, laser-induced heating is compensated by the heat flow towards the low-temperature heat sink. By assuming diffusive phonon transport, the heat conduction equation for a supported 2D material can be written as [43]

$$\frac{1}{r} \frac{d}{dr} \left(r \frac{dT(r)}{dr} \right) - \frac{g}{\kappa t} [T(r) - T_a] + \frac{q_0''}{\kappa t} \exp\left(-\frac{r^2}{r_0^2}\right) = 0. \quad (1)$$

The temperature distribution $T(r)$ in the plane of the 2D material has radial symmetry and a Gaussian profile. Throughout the thickness (t) of the 2D material the same temperature profile is assumed. The layer thicknesses of the mono-, bi-, and trilayer samples used for the calculations are 0.65, 1.4, and 2.4 nm, respectively. The substrate is assumed to be at ambient temperature (T_a) and acts as a heat sink. Here, q_0'' is the peak absorbed laser power per unit area at the center of the beam. The absorbed laser power $Q = q_0'' \pi r_0^2$, where r_0 is the laser beam radius. The laser beam radius for the 50 \times and 100 \times objectives is measured using the modified knife edge method [49] and the values are 0.495 and 0.297 μm , respectively. Details of the laser beam size measurement are included in Sec. S6 of the Supplemental Material [41]. The optical absorption coefficients of mono-, bi-, and trilayer samples are taken as 5.8%, 12.1%, and 17%, respectively. The local temperature rise in the 2D crystal is defined as $\Theta(r) = T(r) - T_a$, and the average temperature rise is given

by

$$\Theta_m(\kappa, g, r_0, Q) = \frac{\int_0^\infty \Theta(r) \exp\left(-\frac{r^2}{r_0^2}\right) r dr}{\int_0^\infty \exp\left(-\frac{r^2}{r_0^2}\right) r dr}. \quad (2)$$

The thermal resistance which impedes the flow of heat in the system is obtained as $R_m = \Theta_m/Q$. The ratio of R_m for two distinct laser beam sizes depends only on the material parameters κ and g . Hence on solving Eq. (1) for two beam sizes, we are able to estimate κ and g uniquely. The estimated in-plane thermal conductivity and interface conductance values, along with the R_m ratios, are presented in Table I. Since the convection through air accounts for less than 0.15% of the total heat conduction, its effect is ignored in the estimation of thermal parameters [26]. The in-plane thermal conductivity decreases as the layer number increases, whereas the total interface conductance per unit area across the 2D material-substrate interface increases. The reduction in in-plane thermal conductivity for an increased layer number is primarily attributed to the intrinsic scattering mechanism of phonons [50].

In this work, the measured value of κ of the monolayer MoS_2 sample is less than the previously reported value of 55 ± 20 W/mK in samples without any structural defects [26]. However, in the case of bilayer samples, our measured value of κ is close to their reported value of 35 ± 7 W/mK [26]. In this context, it is essential to note that our MoS_2 samples contain sulfur vacancies which can alter their thermal transport properties. In our MoS_2 crystals, the additional surface vacancies created during annealing in an Ar/H_2 environment are mostly concentrated on exposed surfaces. Given the monolayer's high surface-to-volume ratio and larger exposed area, it contains the maximum defect density. Consequently, the highest reduction in thermal conductivity due to sulfur vacancies is observed for monolayer samples.

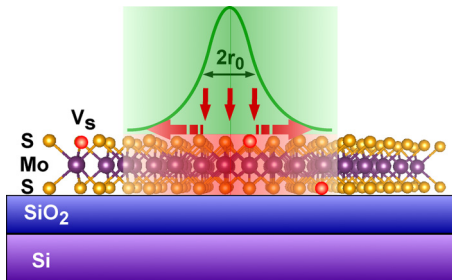


FIG. 5. Schematic of the laser heating and thermal transport in MoS_2 with sulfur vacancies exfoliated on a Si/SiO_2 substrate.

TABLE I. Thermal resistance ratio, in-plane thermal conductivity, and interface thermal conductance (at room temperature) of mono-, bi-, and trilayer MoS_2 crystals on a SiO_2/Si substrate.

Sample	R_m ratio	κ (W/mK)	g ($\text{MW}/\text{m}^2 \text{K}$)
1L	2.282 ± 0.037	$40 + 8 / - 6$	1.02 ± 0.03
2L (2H)	2.137 ± 0.084	$33 + 10 / - 7$	$1.09 + 0.04 / - 0.05$
2L (3R)	2.15 ± 0.13	$32 + 13 / - 10$	$1.07 + 0.13 / - 0.15$
3L (2H)	2.082 ± 0.068	28 ± 6	1.23 ± 0.05

Additionally, as the layer number increases, there might be a reduction in sulfur vacancy density in MoS₂ crystals. Hence, the observed lesser reduction in the thermal conductivity of MoS₂ with sulfur vacancies in crystals with higher layer numbers could be due to their lesser defect density. Our observations align with recent theoretical predictions indicating that the presence of sulfur vacancies substantially reduces the thermal conductivity of monolayer MoS₂ primarily due to strong phonon localization and increased scattering by defects [31,33]. However, the impact of sulfur vacancies on the thermal conductivity of bulk MoS₂ is expected to be less significant due to the lower sulfur vacancy density in bulk crystals compared to monolayer crystals [33]. Additionally, no significant variation is observed in the κ and g values of $2H$ and $3R$ stacked bilayer MoS₂ samples. It is essential to acknowledge that the specific impact of sulfur vacancies on thermal transport in MoS₂ can depend on additional factors such as vacancy type, concentration, and distribution.

III. CONCLUSIONS

In conclusion, we investigated the first-order temperature coefficients of interlayer and intralayer Raman modes of MoS₂ crystals with inherent sulfur vacancies exfoliated on a Si/SiO₂ substrate. Later, the κ and g values of

mono-, bi-, and trilayer MoS₂ crystals were measured using Raman thermometry. The κ value decreased, and the g value increased as the layer number increased. Importantly, we observed that the thermal conductivity is significantly suppressed by sulfur vacancies in monolayer MoS₂. However, this reduction in κ became less evident as the layer number increased. Our results agree with a previous theoretical report that the suppression of thermal transport in MoS₂ by point defects is more prominent in monolayers and becomes negligible as the layer number increases. This lesser reduction in thermal conductivity with increasing layer number could be attributed to the lower sulfur vacancy density at higher layer numbers. No significant variation was observed in the κ and g values of $2H$ and $3R$ stacked bilayer MoS₂ samples.

ACKNOWLEDGMENTS

J.B. acknowledges the financial support from Science and Engineering Research Board (SERB), Govt. of India, through Grant No. CRG/2020/000615. The authors thank the Central Instrumentation Facility (CIF) and Central Micro-Nano Fabrication Facility (CMFF), Indian Institute of Technology Palakkad and Central Instrumentation Facility (CIF), IISER Thiruvananthapuram for the experimental facilities.

-
- [1] K. F. Mak, C. Lee, J. Hone, J. Shan, and T. F. Heinz, Atomically thin MoS₂: A new direct-gap semiconductor, *Phys. Rev. Lett.* **105**, 136805 (2010).
- [2] X. Liu, T. Galfsky, Z. Sun, F. Xia, E.-c. Lin, Y.-H. Lee, S. Kéna-Cohen, and V. M. Menon, Strong light-matter coupling in two-dimensional atomic crystals, *Nat. Photon.* **9**, 30 (2015).
- [3] D. Xiao, G.-B. Liu, W. Feng, X. Xu, and W. Yao, Coupled spin and valley physics in monolayers of MoS₂ and other group-VI dichalcogenides, *Phys. Rev. Lett.* **108**, 196802 (2012).
- [4] K. F. Mak, K. He, J. Shan, and T. F. Heinz, Control of valley polarization in monolayer MoS₂ by optical helicity, *Nat. Nanotechnol.* **7**, 494 (2012).
- [5] H. Zeng, J. Dai, W. Yao, D. Xiao, and X. Cui, Valley polarization in MoS₂ monolayers by optical pumping, *Nat. Nanotechnol.* **7**, 490 (2012).
- [6] P. Chakrabarti, F. Mujeeb, and S. Dhar, Enhancement of valley polarization in CVD grown monolayer MoS₂ films, *Appl. Phys. Lett.* **121**, 072103 (2022).
- [7] M. Buscema, M. Barkelid, V. Zwiller, H. S. van der Zant, G. A. Steele, and A. Castellanos-Gomez, Large and tunable photothermoelectric effect in single-layer MoS₂, *Nano Lett.* **13**, 358 (2013).
- [8] J. Wu, H. Schmidt, K. K. Amara, X. Xu, G. Eda, and B. Özyilmaz, Large thermoelectricity via variable range hopping in chemical vapor deposition grown single-layer MoS₂, *Nano Lett.* **14**, 2730 (2014).
- [9] H. Huang, Y. Cui, Q. Li, C. Dun, W. Zhou, W. Huang, L. Chen, C. A. Hewitt, and D. L. Carroll, Metallic 1T phase MoS₂ nanosheets for high-performance thermoelectric energy harvesting, *Nano Energy* **26**, 172 (2016).
- [10] B. Radisavljevic, A. Radenovic, J. Brivio, V. Giacometti, and A. Kis, Single-layer MoS₂ transistors, *Nat. Nanotechnol.* **6**, 147 (2011).
- [11] Y. Chen, S. Huang, X. Ji, K. Adepalli, K. Yin, X. Ling, X. Wang, J. Xue, M. Dresselhaus, J. Kong, and B. Yildiz, Tuning electronic structure of single layer MoS₂ through defect and interface engineering, *ACS Nano* **12**, 2569 (2018).
- [12] R. Cheng, S. Jiang, Y. Chen, Y. Liu, N. Weiss, H.-C. Cheng, H. Wu, Y. Huang, and X. Duan, Few-layer molybdenum disulfide transistors and circuits for high-speed flexible electronics, *Nat. Commun.* **5**, 5143 (2014).
- [13] M. Fontana, T. Deppe, A. K. Boyd, M. Rinzan, A. Y. Liu, M. Paranjape, and P. Barbara, Electron-hole transport and photovoltaic effect in gated MoS₂ Schottky junctions, *Sci. Rep.* **3**, 1634 (2013).
- [14] T. Pham, G. Li, E. Bekyarova, M. E. Itkis, and A. Mulchandani, MoS₂-based optoelectronic gas sensor with sub-parts-per-billion limit of NO₂ gas detection, *ACS Nano* **13**, 3196 (2019).
- [15] M. Bernardi, M. Palummo, and J. C. Grossman, Extraordinary sunlight absorption and one nanometer thick photovoltaics using two-dimensional monolayer materials, *Nano Lett.* **13**, 3664 (2013).
- [16] L. Sun, C.-Y. Wang, A. Krasnok, J. Choi, J. Shi, J. S. Gomez-Diaz, A. Zepeda, S. Gwo, C.-K. Shih, A. Alù, and X. Li, Separation of valley excitons in a MoS₂ monolayer using a subwavelength asymmetric groove array, *Nat. Photon.* **13**, 180 (2019).
- [17] J. Xu, G. Shao, X. Tang, F. Lv, H. Xiang, C. Jing, S. Liu, S. Dai, Y. Li, J. Luo, and Z. Zhou, Frenkel-defected monolayer

- MoS₂ catalysts for efficient hydrogen evolution, *Nat. Commun.* **13**, 2193 (2022).
- [18] H. Qiu, T. Xu, Z. Wang, W. Ren, H. Nan, Z. Ni, Q. Chen, S. Yuan, F. Miao, F. Song *et al.*, Hopping transport through defect-induced localized states in molybdenum disulfide, *Nat. Commun.* **4**, 2642 (2013).
- [19] R. J. Toh, Z. Sofer, J. Luxa, D. Sedmidubsky, and M. Pumera, 3R phase of MoS₂ and WS₂ outperforms the corresponding 2H phase for hydrogen evolution, *Chem. Commun.* **53**, 3054 (2017).
- [20] J. Shi, P. Yu, F. Liu, P. He, R. Wang, L. Qin, J. Zhou, X. Li, J. Zhou, X. Sui *et al.*, 3R MoS₂ with broken inversion symmetry: A promising ultrathin nonlinear optical device, *Adv. Mater.* **29**, 1701486 (2017).
- [21] H. Hallil, W. Cai, K. Zhang, P. Yu, S. Liu, R. Xu, C. Zhu, Q. Xiong, Z. Liu, and Q. Zhang, Strong piezoelectricity in 3R-MoS₂ flakes, *Adv. Electron. Mater.* **8**, 2101131 (2022).
- [22] W. Zhou, X. Zou, S. Najmaei, Z. Liu, Y. Shi, J. Kong, J. Lou, P. M. Ajayan, B. I. Yakobson, and J.-C. Idrobo, Intrinsic structural defects in monolayer molybdenum disulfide, *Nano Lett.* **13**, 2615 (2013).
- [23] S. Tongay, J. Suh, C. Ataca, W. Fan, A. Luce, J. S. Kang, J. Liu, C. Ko, R. Raghunathanan, J. Zhou *et al.*, Defects activated photoluminescence in two-dimensional semiconductors: Interplay between bound, charged and free excitons, *Sci. Rep.* **3**, 2657 (2013).
- [24] R. Yan, J. R. Simpson, S. Bertolazzi, J. Brivio, M. Watson, X. Wu, A. Kis, T. Luo, A. R. Hight Walker, and H. G. Xing, Thermal conductivity of monolayer molybdenum disulfide obtained from temperature-dependent Raman spectroscopy, *ACS Nano* **8**, 986 (2014).
- [25] S. Sahoo, A. P. S. Gaur, M. Ahmadi, M. J.-F. Guinel, and R. S. Katiyar, Temperature-dependent Raman studies and thermal conductivity of few-layer MoS₂, *J. Phys. Chem. C* **117**, 9042 (2013).
- [26] X. Zhang, D. Sun, Y. Li, G.-H. Lee, X. Cui, D. Chenet, Y. You, T. F. Heinz, and J. C. Hone, Measurement of lateral and interfacial thermal conductivity of single- and bilayer MoS₂ and MoSe₂ using refined optothermal Raman technique, *ACS Appl. Mater. Interfaces* **7**, 25923 (2015).
- [27] P. Yuan, R. Wang, T. Wang, X. Wang, and Y. Xie, Nonmonotonic thickness-dependence of in-plane thermal conductivity of few-layered MoS₂: 2.4 to 37.8 nm, *Phys. Chem. Chem. Phys.* **20**, 25752 (2018).
- [28] Z. Ding, Q.-X. Pei, J.-W. Jiang, and Y.-W. Zhang, Manipulating the thermal conductivity of monolayer MoS₂ via lattice defect and strain engineering, *J. Phys. Chem. C* **119**, 16358 (2015).
- [29] B. Peng, Z. Ning, H. Zhang, H. Shao, Y. Xu, G. Ni, and H. Zhu, Beyond perturbation: Role of vacancy-induced localized phonon states in thermal transport of monolayer MoS₂, *J. Phys. Chem. C* **120**, 29324 (2016).
- [30] D. Saha and S. Mahapatra, Theoretical insights on the electrothermal transport properties of monolayer MoS₂ with line defects, *J. Appl. Phys.* **119**, 134304 (2016).
- [31] Y. Wang, K. Zhang, and G. Xie, Remarkable suppression of thermal conductivity by point defects in MoS₂ nanoribbons, *Appl. Surf. Sci.* **360**, 107 (2016).
- [32] C. Lin, X. Chen, and X. Zou, Phonon-grain-boundary-interaction-mediated thermal transport in two-dimensional polycrystalline MoS₂, *ACS Appl. Mater. Interfaces* **11**, 25547 (2019).
- [33] C. A. Polanco, T. Pandey, T. Berlijn, and L. Lindsay, Defect-limited thermal conductivity in MoS₂, *Phys. Rev. Mater.* **4**, 014004 (2020).
- [34] K. Xu, T. Liang, Z. Zhang, X. Cao, M. Han, N. Wei, and J. Wu, Grain boundary and misorientation angle-dependent thermal transport in single-layer MoS₂, *Nanoscale* **14**, 1241 (2022).
- [35] A. J. Gabourie, S. V. Suryavanshi, A. B. Farimani, and E. Pop, Reduced thermal conductivity of supported and encased monolayer and bilayer MoS₂, *2D Mater.* **8**, 011001 (2021).
- [36] Y. Zhao, M. Zheng, J. Wu, X. Guan, A. Suwardi, Y. Li, M. Lal, G. Xie, G. Zhang, L. Zhang, and J. T. L. Thong, Modification of thermal transport in few-layer MoS₂ by atomic-level defect engineering, *Nanoscale* **13**, 11561 (2021).
- [37] M. Yarali, X. Wu, T. Gupta, D. Ghoshal, L. Xie, Z. Zhu, H. Brahmi, J. Bao, S. Chen, T. Luo *et al.*, Effects of defects on the temperature-dependent thermal conductivity of suspended monolayer molybdenum disulfide grown by chemical vapor deposition, *Adv. Funct. Mater.* **27**, 1704357 (2017).
- [38] J. Hong, Z. Hu, M. Probert, K. Li, D. Lv, X. Yang, L. Gu, N. Mao, Q. Feng, L. Xie *et al.*, Exploring atomic defects in molybdenum disulfide monolayers, *Nat. Commun.* **6**, 6293 (2015).
- [39] Y. Zhu, J. Lim, Z. Zhang, Y. Wang, S. Sarkar, H. Ramsden, Y. Li, H. Yan, D. Phuyal, N. Gauriot *et al.*, Room-temperature photoluminescence mediated by sulfur vacancies in 2D molybdenum disulfide, *ACS Nano* **17**, 13545 (2023).
- [40] M. K. Ranjuna and J. Balakrishnan, High temperature anomalous Raman and photoluminescence response of molybdenum disulfide with sulfur vacancies, *Sci. Rep.* **13**, 16418 (2023).
- [41] See Supplemental Material at <http://link.aps.org/supplemental/10.1103/PhysRevB.108.245411> for the layer number and stacking order determination, temperature coefficients of low-frequency Raman modes, layer number dependent power coefficients, estimation of κ and g , variation of κ and g with layer number and stacking order, discussion on substrate heating, laser beam size determination, and TEM characterization, which includes Ref. [42].
- [42] J. van Baren, G. Ye, J.-A. Yan, Z. Ye, P. Rezaie, P. Yu, Z. Liu, R. He, and C. H. Lui, Stacking-dependent interlayer phonons in 3R and 2H MoS₂, *2D Mater.* **6**, 025022 (2019).
- [43] W. Cai, A. L. Moore, Y. Zhu, X. Li, S. Chen, L. Shi, and R. S. Ruoff, Thermal transport in suspended and supported monolayer graphene grown by chemical vapor deposition, *Nano Lett.* **10**, 1645 (2010).
- [44] H. Li, Q. Zhang, C. C. R. Yap, B. K. Tay, T. H. T. Edwin, A. Olivier, and D. Baillargeat, From bulk to monolayer MoS₂: Evolution of Raman scattering, *Adv. Funct. Mater.* **22**, 1385 (2012).
- [45] H. Kim, H. Ko, S. M. Kim, and H. Rho, Temperature dependent Raman spectroscopy of shear and layer breathing modes in bilayer MoS₂, *Curr. Appl. Phys.* **25**, 41 (2021).

- [46] I. Maity, P. K. Maiti, and M. Jain, Temperature-dependent layer breathing modes in two-dimensional materials, *Phys. Rev. B* **97**, 161406(R) (2018).
- [47] J. Judek, A. P. Gertych, M. Świniarski, A. Łapińska, A. Dużyńska, and M. Zdrojek, High accuracy determination of the thermal properties of supported 2D materials, *Sci. Rep.* **5**, 12422 (2015).
- [48] S. M. H. Goushehgir, Simple exact analytical solution of laser-induced thermal transport in supported 2D materials, *Int. Commun. Heat Mass Transfer* **128**, 105592 (2021).
- [49] A. Taube, J. Judek, A. Łapinska, and M. Zdrojek, Temperature-dependent thermal properties of supported MoS₂ monolayers, *ACS Appl. Mater. Interfaces* **7**, 5061 (2015).
- [50] E. Easy, Y. Gao, Y. Wang, D. Yan, S. M. Goushehgir, E.-H. Yang, B. Xu, and X. Zhang, Experimental and computational investigation of layer-dependent thermal conductivities and interfacial thermal conductance of one-to three-layer WSe₂, *ACS Appl. Mater. Interfaces* **13**, 13063 (2021).